Received: 8 May 2025 | Revised: 24 September 2025 | Accepted: 28 September 2025

DOI: 10.1002/mp.70080

RESEARCH ARTICLE

MEDICAL PHYSICS

Seven-probe fiber detector for time-resolved source tracking in HDR-brachytherapy: Pre-clinical experimental evaluation

Mathieu Gonod[1] | **Miguel Angel Suarez**[2] | **Samir Laskri**[3] | **Gwenaël Rolin**[4] | **Karine Charriere**[5] | **Emmanuel Dordor**[2] | **Julien Crouzilles**[3] | **Thomas Lihoreau**[6] | **Lionel Pazart**[5] | **Jean-François Vinchant**[3] | **Léone Aubignac**[1] | **Thierry Grosjean**[2]

[1]Medical physics department, Centre Georges François Leclerc (CGFL) - Dijon, Dijon, France

[2]Marie and Louis Pasteur University, CNRS, FEMTO-ST Institute, Besançon, France

[3]SEDI-ATI Fibres Optiques, Évry-Courcouronnes, France

[4]Marie and Louis Pasteur University, CHU, UMR INSERM 1098 RIGHT, INSERM11 CIC1431, Besançon, France

[5]UMR INSERM 1322 LINC, INSERM CIC1431, Université Marie et Louis Pasteur, CHU Besançon, Besançon, France

[6]INSERM CIC1431, SINERGIES (UR4662), 15 Tech4Health network (F-CRIN), Université Marie et Louis Pasteur, CHU Besançon, Besançon, France

Correspondence
Thierry Grosjean, Université Marie et Louis Pasteur, CNRS, Intitut FEMTO-ST, F-25000 Besançon, France.
Email: thierry.grosjean@univ-fcomte.fr

Funding information
Agence Nationale de la Recherche, Grant/Award Number: ANR-18-CE42-0016; SATT SAYENS; EIPHI Graduate School, Grant/Award Number: ANR-17-EURE-0002; Equipex+ SMARTLIGHT Platform, Grant/Award Number: ANR-21-ESRE-0040; Equipex+ NANOFUTUR, Grant/Award Number: ANR-21-ESRE-0012; RENATECH Network; Region Bourgogne Franche-Comte

Abstract

Background: In vivo dosimetry (IVD) is increasingly recognized as a critical tool for verifying treatment delivery in HDR-brachytherapy (HDR-BT). Time-resolved techniques, such as source tracking, enable real-time error detection and reduce uncertainties in dose delivery. However, to date, multichannel detection systems have been tested only in limited conditions that do not reflect the full diversity of clinical HDR-BT scenarios.

Purpose: This study evaluates a compact biocompatible Seven-probe Scintillator Detector (7SD) for monitoring HDR-BT treatment sequences across a range of dwell times and source-probe spacings representative of most HDR-BT techniques. The capability of the 7SD to detect source insertion errors is also assessed.

Methods: The 7SD comprises seven detection cells made of Gd_2O_2S:Tb, each measuring 0.28 $\pm$ 0.02 mm in diameter and 0.43 $\pm$ 0.02 mm in length, coupled to the microstructured tips of silica optical fibers (110-micron diameter). The probes, spaced 15 mm apart along the fiber axis, are organized into a bundle with a total diameter of less than 0.45 mm. The 7SD was tested in a $50 \times 50 \times 30$ cm^3 phantom using a MicroSelectron 9.1 Ci Ir-192 HDR afterloader connected to a BT stainless steel interstitial needle. Detection signals were acquired at 0.06-second intervals with an sCMOS camera equipped with a chromatic filter to eliminate spurious Cerenkov signals. The probe was experimentally calibrated in 2D without relying on the AAPM-TG43 formalism. Monitoring of dwell times and positions was performed by combining detection signals from all seven probes. Cytotoxicity tests were performed to confirm the biocompatibility of the 7SD

Results: A total of 4040 dwell positions were analyzed, covering source-probe spacings from 10 to 36 mm and a source travel range of 62 mm, with dwell times ranging from 0.1 to 19.5 s. The 7SD successfully identified 99.5% of the dwell positions. In cylindrical coordinates, the measured dwell positions deviated from the planned values by 0.224 $\pm$ 0.155 mm (radial) and 0.077 $\pm$ 0.181 mm (axial, source travel axis). The average deviation from planned dwell times was 0.006 $\pm$ 0.061 s. 99.4% of the dwell positions were measured within the 1 mm reliability threshold. The remaining 0.6% of deviations consistently occurred at the initial dwell position of treatment sequences and appear to stem from a systematic source positioning error by the afterloader. Additionally, the detector accurately identified intentional needle mispositioning scenarios with sub-millimeter accuracy.

Conclusions: A 7SD based on Gd_2O_2S:Tb, coupled with an sCMOS camera, demonstrates its suitability for time-resolved IVD in monitoring HDR-BT treatments. The 7SD substantially extends the monitoring volume along both the source's axial path and the orthogonal radial direction, enabling accurate source tracking across treatment geometries representative of a wide variety of HDR-BT procedures. By detecting subtle afterloader malfunctions, the 7SD offers a precise and valuable means of evaluating the integrity of HDR-BT setups and procedures. Its high-resolution monitoring capabilities, confirmed biocompatibility, scalability, and compatibility with standard BT needles, catheters, and applicators underscore its potential for clinical implementation.

KEYWORDS
HDR-brachytherapy, dwell time and position verification, seven-probe detector

1 | INTRODUCTION

High-dose-rate brachytherapy (HDR-BT) is a widely used radiotherapy technique that delivers high doses of radiation in close proximity to the tumor while sparing surrounding healthy tissues. By using a temporary radioactive source, such as Iridium-192, positioned precisely within or near the tumor via applicators, catheters or needles, HDR-BT achieves exceptional dose localization and treatment efficacy, making it a standard approach for cancers like prostate, cervical, and breast cancer. However, the high precision required in HDR-BT also makes it susceptible to potential errors, such as incorrect source positioning, dwell time deviations, or applicator misplacement. These errors can lead to suboptimal dose delivery, resulting in reduced treatment efficacy or unintended exposure to healthy tissues. Given the high dose gradients involved and the proximity to critical organs, even small deviations can have significant clinical consequences.

To address these challenges, in vivo dosimetry (IVD) has emerged as a promising tool for real-time verification of treatment delivery [1,2]. IVD enables direct monitoring of dose delivery during the procedure, providing immediate feedback on the treatment. This capability enhances patient safety by promptly identifying and correcting errors, ensuring optimal therapeutic outcomes. Integrating a scintillating cell with an optical fiber has shown considerable potential for developing compact detectors capable of time-resolved monitoring of dwell times, source positions, and/or delivered doses [3–12]. Moreover, by comparing measured dose values to those predicted by the treatment planning system (TPS), some source insertion errors have been successfully determined [10]. However, these single-probe detectors are constrained by a limited monitoring volume.

Integrating multiple detection sites into a single BT needle or catheter is essential for expanding the monitoring volume along the source's travel range, while enabling precise real-time treatment delivery monitoring in 2D or 3D. One approach utilizes arrays of independent fiber-based scintillation detectors [13–15]. Another strategy integrates up to three scintillation cells into a single optical fiber, enabling multiple detection points within a single BT needle or catheter to monitor dose deposition [16,17], as well as dwell times and dwell positions [18]. These multipoint detectors have demonstrated time-resolved two-dimensional (2D) source tracking through triangulation techniques [18]. An evolution of this technology combines a three-point detector [18] with a single-probe dosimeter, each integrated into a distinct BT needle, to enable three-dimensional (3D) source position tracking through inter-probe triangulation [19]. Building on advances in miniaturization, a six-probe detector was recently developed, compact enough to be integrated into standard BT needles or catheters [20]. This architecture enables versatile monitoring strategies while simplifying in vivo detection schemes and improving spatial accuracy.

Despite these advances, performance evaluations of multipoint and multiprobe systems have so far been limited to treatment sequences with dwell times of one second or longer, excluding the short dwell times commonly encountered in prostate HDR-BT. Moreover, most previous studies have focused on one-dimensional (1D) tracking of the source along its axial path [13–17,20]. Although 2D source tracking via triangulation has been demonstrated, it has only been validated in highly constrained treatment sequences involving source-detector spacings of 5 mm, which do not reflect the full diversity of clinical practice [18]. To fully unlock the clinical potential of these multichannel detection systems, a more comprehensive assessment of their multidimensional tracking capabilities is needed under a wider variety of HDR-BT conditions. This includes validating their performance across a broader range of dwell times, down to 0.1 s, and source-probe spacings extending up to several centimeters. Such an investigation is crucial to confirm their reliability, spatial accuracy, and clinical applicability. Additionally, assessing the detectors' ability to identify and quantify source insertion errors, such as axial shifts or angular misalignmentsis essential to ensure safe and precise treatment delivery.

This study introduces and evaluates a biocompatible Seven-probe Scintillator Detector (7SD) for monitoring HDR-BT treatment sequences with dwell times ranging from 0.1 to 19.5 s. The 7SD substantially increases the monitoring volume along both the axial displacement of the HDR-BT source and the orthogonal radial direction, facilitating precise tracking over a wide variety of treatments. The 7SD was encapsulated in a rigid, biocompatible plastic tube with an outer diameter similar to that of standard prostate HDR-BT needles. With a total diameter of less than 0.45 mm, the 7SD is compact enough to be integrated into most HDR-BT needles and catheters, making it suitable for a wide range of clinical applications. The probe assessment focuses on the time-resolved measurement of the (r, z) coordinates of the source for 2D source tracking, dwell time measurement, and the dwell position identification rate as a function of dwell time. The reliability level of the 7SD in monitoring dwell position was also studied. Additionally, the detector's ability to detect source insertion errors was evaluated under conditions of needle mispositioning (axial shifts along the $(0z)$ axis) and misalignment (source needle tilt relative to the detector).

2 | MATERIALS AND METHODS

2.1 | The 7-probe detector

2.1.1 | 7SD design and structure

The 7SD consists of seven independent inorganic scintillating microcells grafted at the tips of seven biocompatible optical fibers forming a 10-meter-long hexagonal-lattice bundle. Each fiber has an outer diameter of 110 microns (with a 100-micron core) and is coated with an 8-micron-thick polyimide protective layer. The combined fiber bundle has a total diameter of 375 microns. Gd_2O_2S:Tb was selected as the scintillator due to its high luminescence efficiency, stability, linearity, and fast temporal response [21–23]. Additionally, Gd_2O_2S:Tb exhibits low sensitivity to temperature variations in the range of 15°C–40°C [24,25].

To enhance the transfer of luminescence from the scintillators to the guided modes of the optical fibers, each fiber tip was tapered into a controlled shape, serving as an optical analog of a leaky-wave antenna [26]. Details of the probe fabrication process have been described in previous works [12,27]. The lengths of the fibers within the bundle were adjusted to maintain a uniform spacing of 15.0 ± 0.1 mm between successive scintillating cells (Figure 1a). The probes are evenly distributed over a 90 mm span. Each scintillation cell has a diameter of 0.28 ± 0.02 mm and a length of 0.43 ± 0.02 mm, resulting in a detection volume of less than 0.02 mm^3 (Figure 1b). The diameter of the 7SD structure locally increases to approximately 0.41 mm at the position of the scintillating cells.

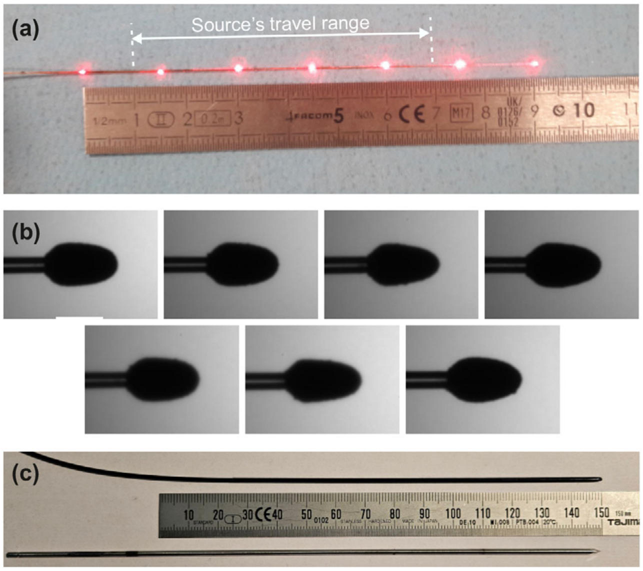

FIGURE 1 The 7SD. (a) Photograph of the 7SD, with the source travel range considered in this study indicated. (b) Microscope images showing the seven tip-integrated scintillation micro-cells composing the 7SD. (c) Photograph of the encapsulated 7SD alongside a commercial HDR-BT interstitial metallic needle for size comparison.

2.1.2 | Encapsulation

The 7SD is encapsulated in a biocompatible soft plastic tube that provides both optical and mechanical shielding. The final 12.5 cm of the encapsulation consists of a biocompatible rigid tube that securely houses the seven scintillation cells. The outer diameter of the encapsulated probe, measuring 1.65 mm, is closely matched to the 1.9-mm-outer-diameter stainless steel interstitial needles (Figure 1c). It is well-suited for insertion through a commercial prostate HDR-BT template. This compact design allows the 7SD to be seamlessly integrated into standard clinical HDR-BT procedures, ensuring compatibility with commercial HDR-BT catheters, needles and applicators.

2.1.3 | Cytotoxicity assessment

Cytotoxicity assessment was performed according to ISO 10993-5 guidelines using the extract method and the MTT assay. To this aim, L929 murine fibroblasts were exposed for 24 h to conditioned media from either an intact or a degraded probe. Briefly, probes were sterilized with ethanol and dry before immersion in culture medium (1 mL, 37°C, 24 h). For the degraded condition,

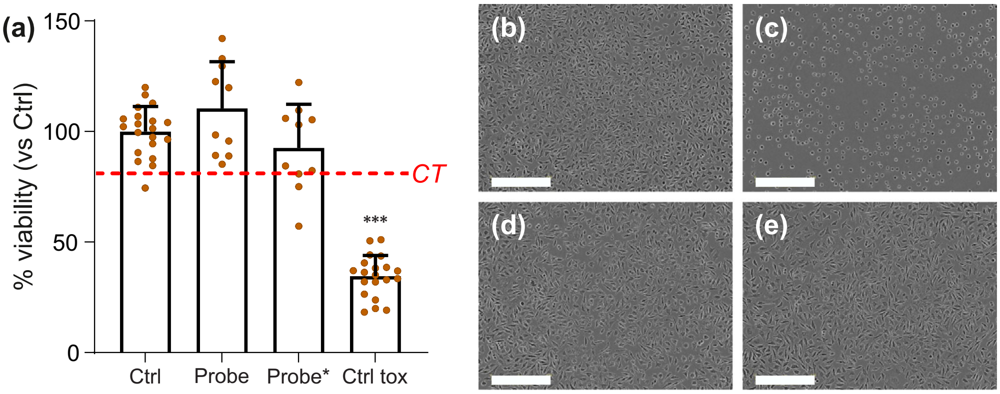

FIGURE 2 Evaluation of the cytotoxicity potential of the intact or degraded probe. (a) Cell viability, measured by MTT assay after 24 h of culture, was compared to negative (Ctrl) and positive (Ctrl tox) controls ($n = 5$, $N = 2$). Statistics: one-way ANOVA with Dunnett's test (*** $p < 0.001$). CT: threshold of 70% for cytotoxicity. (d) and (e) Cell morphology after 24 h of culture in conditioned medium, compared to negative (b) and positive (c) controls: (d) Intact probe, (e) degraded probe. Images were captured using the Incucyte S3 microscope (x10). Scalebar: 0.4 mm

mechanical breakage was applied to the probe before immersion. Then, L929 cells were cultured in the presence of conditioned media during 24 h. Cell viability was quantified by measuring optical density after MTT reduction and expressed as a percentage of untreated controls, with a cytotoxic reference (DMSO 10%). A viability below 70% was considered as cytotoxic.

Results showed that cell viability remained above 70% when cells are cultured in the presence of conditioned media from intact or degraded probe (Figure 2a). Such results indicate that no significant cytotoxicity were detected. Morphological analysis confirmed the absence of structural alterations or vacuolization in treated cells compared to the negative control, while the positive control exhibited clear signs of cytotoxicity (see Figure 2b–e).

Given that the materials used for encapsulating the probe and the adhesive are already established as biocompatible, and considering the challenges faced in degrading the outer capsule to assess the cytotoxicity of the Gd_2O_2S:Tb scintillator, further testing is not warranted. This process provided a preliminary evaluation of the biocompatibility of the 7SD, confirming its safety for potential clinical use.

2.1.4 | Optical readout system

The encapsulated 7SD was connected to a simple yet effective optical readout system, consisting of an sCMOS camera (Andor Technology, Zyla 4.2 model), a camera objective (Fujinon HF35SA), and a chromatic bandpass filter (Semrock) placed in front of the camera. This setup images the output face of the 7SD while simultaneously filtering out spurious Cerenkov signals (stem effect) [12,20,27]. The system operates at a sampling rate τ of 0.06 s, as described in previous work [20].

To facilitate real-time acquisition, a custom LabVIEW-based software platform was developed to control the camera. The software automatically defines 16-pixel-diameter Regions of Interest (ROIs) that enclose the seven hexagonally-arranged light spots observed in the images. Image pixels within each ROI were integrated to generate seven independent detection signals, one per probe, sampled at 0.06-s intervals (τ). This automated process enables continuous tracking of scintillation signals during HDR-BT treatment.

2.2 | The measurement setup

Treatment monitoring was conducted in a 50 x 50 x 30 cm^3 water tank. Irradiation was performed using a MicroSelectron Ir-192 HDR afterloader (9.1 Ci, air kerma strength: 37176 U) connected to a 20 cm stainless steel interstitial needle from Elekta. The needle was positioned in the water tank using a custom-built organic holder consisting of two solid-water needle insertion templates, spaced 13.5 cm apart. Each template features a 12×13 array of 5-mm-spaced holes, patterned according to the grid layout of a commercial prostate stepper template from Elekta. To facilitate the identification of source and detector insertion points, the front plate of the commercial prostate stepper template was mounted on top of the upper solid-water template. The plate's labeled coordinate system, using letters and numbers, provided a standard reference for needle positioning and alignment. To better approach clinical HDR-BT treatment conditions, the front plate was positioned to extend above the water surface. The bottom side of the lower solid-water template was placed in contact with an unprocessed solid-water plate, ensuring that the tips of the source needle and encapsulated probe were aligned at the same height. Images of the

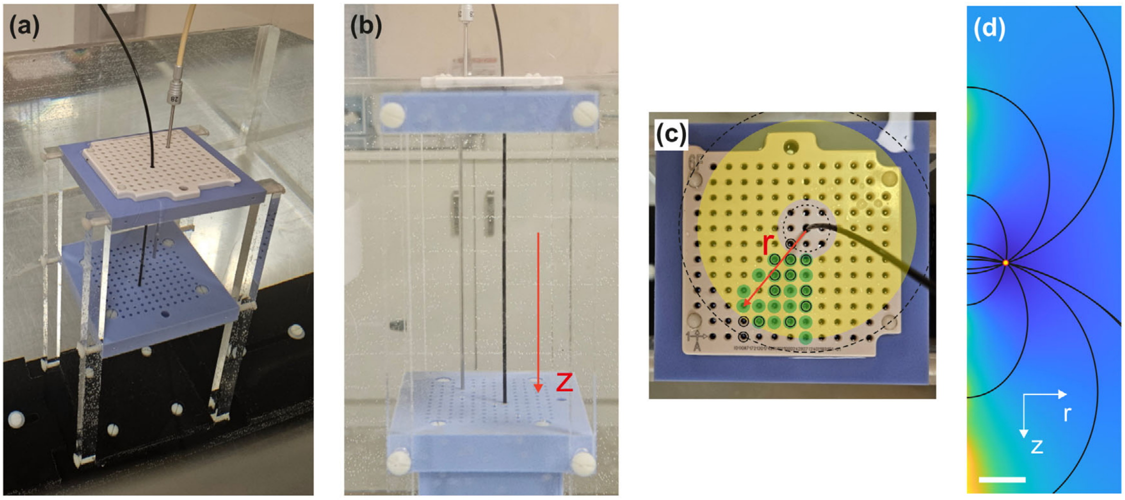

FIGURE 3 (a) Photograph of the measurement setup inside the water tank. (b) Side view of the inter-template region, showing that the source needle and the 7SD are parallel and vertically aligned along the z-axis. (c) Photograph of the top template, where the source insertion holes used for the 7SD calibration and treatment deliveries are marked with black circles and green disks, respectively. The r coordinate is also superimposed on the image. (d) Illustration of the triangulation process used for 2D source positioning at an instant $k\tau$ ($k \in \mathbb{N}$). The seven black elliptical arcs represent the minima of the $\Delta V_i(r, z, k\tau)$ function (Equation 2) for each of the seven probes of the 7SD. The false-color map in the background corresponds to the summation of the seven $\Delta V_i(r, z, k\tau)$ functions, producing a single minimum point at the intersection of the seven positional ellipses. This minimum, marked by a yellow point, determines the source's location in the (r, z) plane.

holder are presented in Figure 3a–c. During calibration and treatment measurements, the 7SD is positioned in the insertion hole H8 (see Figure 3c).

During treatment delivery, the source is initially positioned at the deepest location within the water tank, near the bottom solid-water template, and is then retracted toward the water surface in 2.5 mm steps.

2.3 | System calibration

Optical signals from the scintillators were recorded simultaneously and processed post-irradiation. The signals were converted into 2D source coordinates using calibration plots. The rotationally invariant response of the probes in the 7SD [27] allows detector calibration to be performed using insertion holes located within a limited portion of the template: specifically, within a right triangle covering one-eighth of its area. Thirteen holes within this region were empirically selected (marked with black circles in Figure 3c) to achieve a nearly uniform distribution of source-probe spacings r. Assuming axis symmetry in the environment surrounding the detector, a 2D array of signals corresponding to (r, z) positions was defined for each of the seven probes of the 7SD by merging these 13 acquisition sequences. The z-axis (see Figure 3b) was gridded according to the dwell step size, while the r-axis (cf. Figure 3c) followed the grid layout of the source insertion templates. This configuration of 13 acquisitions provided adequate sampling of the calibration plots. Future investigations could explore how the number of insertion holes affect the accuracy of source position determination. To generate smooth and continuous calibration plots, the measured data were interpolated using the `interp` function in Matlab, yielding a sampling rate of 0.1 mm. The resulting seven calibration plots span 10 cm along the z-axis and extend up to 40 mm from the detector along the r-axis. Owing to axial symmetry, the detector calibration encompasses the region outlined by the two dashed lines in Figure 3c.

2.4 | Treatment plan

The irradiation protocol used to evaluate the 7SD is summarized in Table 1. This protocol combines five distinct prostate HDR-BT treatment plans, each comprising 10 to 16 treatment sequences conducted in separate implanted needles (see the third column of Table 1). These treatment plans reflect the standard clinical practices of the medical center involved in this HDR brachytherapy study and include dwell times as short as 0.1 s. Unlike standard prostate HDR-BT, all treatment sequences within a single plan are executed within the same needle. Each treatment plan is repeated four or five times, with the source needle positioned at different distances (r_{TPS}) from the detector within the plane of the template (cf. Figure 3c). The detector was kept in a fixed position throughout the entire experimental procedure. For each treatment plan, the values of r_{TPS} are provided in the second column of Table 1. The 21 source needle positions, combined across all five treatment plans, are marked with green disks in Figure 3c. The total number of dwell positions for each plan is listed in the last column of Table 1. Repeating each treatment plan 4–5 times across the different source-probe spacings

TABLE 1 Irradiation protocol used to evaluate the performance of the 7SD.

TP	r_{TPS} (mm)					Number of sequences	Total number of dwells
1	15.8	20.6	28.3	31.6	—	16	896
2	14.1	18	26.9	30	—	13	676
3	11.8	22.4	25.5	29.2	—	15	960
4	15	20	30.4	33.5	—	15	828
5	10	21.2	25	32	36	10	680
Total						69	4040

Abbreviation: TP, treatment plan.

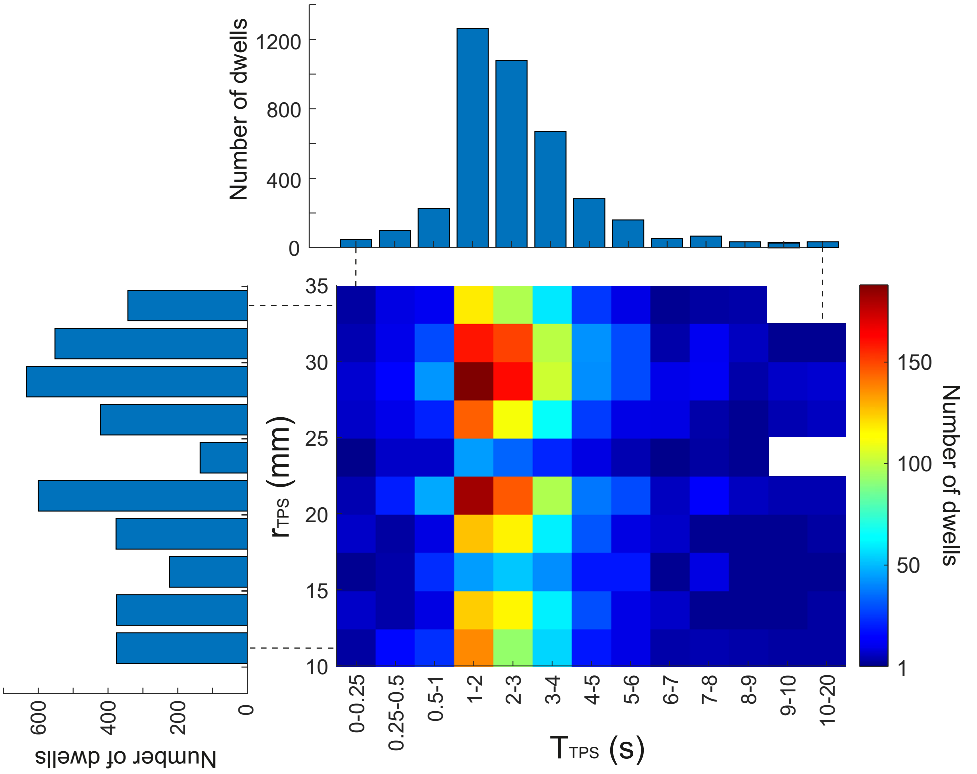

FIGURE 4 Distribution of dwell positions as a function of the planned source-probe spacing (r_{TPS}) and planned dwell time (T_{TPS}).

r listed in Table 1 resulted in a cumulative total of 4040 dwell positions. These positions span nearly all combinations of source-probe spacings and dwell times investigated in this study, with a minimum of 120 dwell positions recorded for each spacing (see Figure 4).

By symmetry, the evaluation area, highlighted in yellow in Figure 3c, extends 36 mm in all directions around the detector.

2.5 | 2D source position tracking using the 7SD system

During treatment delivery, each probe P_i ($i = [1, 7]$) of the 7SD system generates a staircased temporal electric signal $V_i(t)$ sampled at fixed time intervals $\tau = 0.06$ s. At each time instant $t = k\tau$, where $k \in \mathbb{N}$, the 2D coordinates (r_S, z_S) of the source position are determined using the following equation:

$$f(r, z, k\tau) = \sum_{i=1}^{7} \Delta V_i(r, z, k\tau), \qquad (1)$$

where:

$$\Delta V_i(r, z, k\tau) = \frac{|C_i(r, z) - \varkappa V_i(k\tau)|}{max(C_i(r, z))}. \qquad (2)$$

Here, $\varkappa$ is a normalization coefficient that compensates for difference in source activity between the calibration and treatment phases. The function $\Delta V_i(r, z, k\tau)$ represents the normalized deviation of the measured signal $V_i(k\tau)$ from the renormalized calibration map $C_i(r, z)$ for each probe. The 2D source position (r_S, z_S) at time $k\tau$ is obtained by identifying the minimum of the composite function $f(r, z, k\tau)$ (Equation 1). Each probe P_i corresponds to an individual function $\Delta V_i(r, z, k\tau)$ (Equation 2) whose minimum, ideally zero, defines an elliptical isoprobability contour indicating potential source locations at time $k\tau$. By applying a triangulation method, the sum of the seven $\Delta V_i(r, z, k\tau)$ functions yields a single minimum point corresponding to the intersection of these elliptical contours, thereby providing the source's position. This triangulation procedure is illustrated in Figure 3d.

During treatment, the source moves between successive dwell positions within a time frame of a few tens of milliseconds [28]. This movement introduces transient phases in the staircase-shaped readout signals, which typically last for one or two acquisition points. To avoid these transient signals in the dwell position analysis, the first and last acquisition points at each dwell position are systematically excluded from the source tracking process.

2.6 | Dwell time measurement

The dwell time corresponds to the interval between two successive transient phases in the temporal readout signals. It is determined using an edge detection algorithm applied to each probe's readout signal, $V_i(k\tau)$ [29]. The algorithm involves independently convolving each signal $V_i(k\tau)$ with a filter characterized by an impulse response composed of two rectangular functions with opposite signs [29]. This yields seven convolution functions, each displaying a series of narrow peaks. These functions are then summed to produce a combined signal, from which dwell times are extracted as the time intervals between successive peaks. By integrating the signals from all seven probes, the method improves edge detection precision and robustness, reducing the impact of noise from individual probes.

2.7 | Reliability analysis

The reliability of the 7SD in tracking a HDR-BT source was evaluated by analyzing the rate of detected dwell positions whose overall offset from the planned dwell positions does not exceed 1 mm. This confidence criterion aligns with the positional accuracy tolerances for the source and X-ray marker, as well as the length tolerances of applicators or treatment tubes, in both HDR and PDR brachytherapy. [30].

2.7.1 | Systematic reliability analysis

A systematic reliability analysis of the system was performed by recording signals from the 7SD as the source was incrementally moved along the z-axis within the treatment region. The irradiation procedure consisted of 12 dwell positions spaced 2.5 mm apart, with a dwell time of 10 seconds at each position. This process was repeated for 12 different source-probe spacings, r, ranging from 10 to 36 mm. Using the algorithm detailed in Section 2.5, the distance $R = \sqrt{(r_{TPS} - r_s)^2 + (z_{TPS} - z_s)^2}$ between the planned and measured instantaneous source positions was computed as a function of time for the 12 source-probe spacing values. This process yielded 12 time traces of the distance R to the planned source positions, sampled at 0.06-s intervals. Each of these time traces was subsequently resampled 30 times over fixed time intervals, which incrementally increased from 0.1 s to 3 s. As a result, for each source-probe spacing r, 30 distributions of source-probe position deviations, $\bar{R}$, integrated over time intervals Δt ranging from 0.1 to 3 s, were generated. For each combination of source-probe spacing r and integration interval Δt, the fraction of $\bar{R}$-values that fell within the reliability criterion of 1 mm was analyzed.

2.7.2 | Treatment plan analysis

The overall offset, R_{dwell}, between the measured and planned dwell positions, $(\bar{r}_s, \bar{z}_s)$ and (r_{TPS}, z_{TPS}), respectively, is computed as $R_{dwell} = \sqrt{(r_{TPS} - \bar{r}_s)^2 + (z_{TPS} - \bar{z}_s)^2}$.

2.8 | Detection of treatment needle mispositioning

To evaluate the ability of the 7SD to detect errors in source needle positioning, two types of deliberate mispositioning scenarios were introduced: a shift of the source needle along its insertion axis z and a tilt relative to the z-axis. In the first scenario, the source shift was manually displaced by 1, 2, or 3 mm along the z-axis. Measurements were performed at a source-probe spacing $r = 22.4$ mm. In the second scenario, the source needle was misaligned by inserting it into two different neighboring holes in the upper and lower solid-water needle insertion templates.

For both the shift and tilt error analyses, a sequence of 26 dwell positions was investigated, each with a dwell time of 3.7 s and spaced 2.5 mm apart. This configuration spanned a 62 mm segment along the z-axis, matching the treatment region examined in the other characterizations.

3 | RESULTS

3.1 | Dwell identification

Overall, 99.5% of the dwell positions were successfully identified (see Table 2). Notably, all source positions with dwell times of 0.2 seconds or longer were accurately

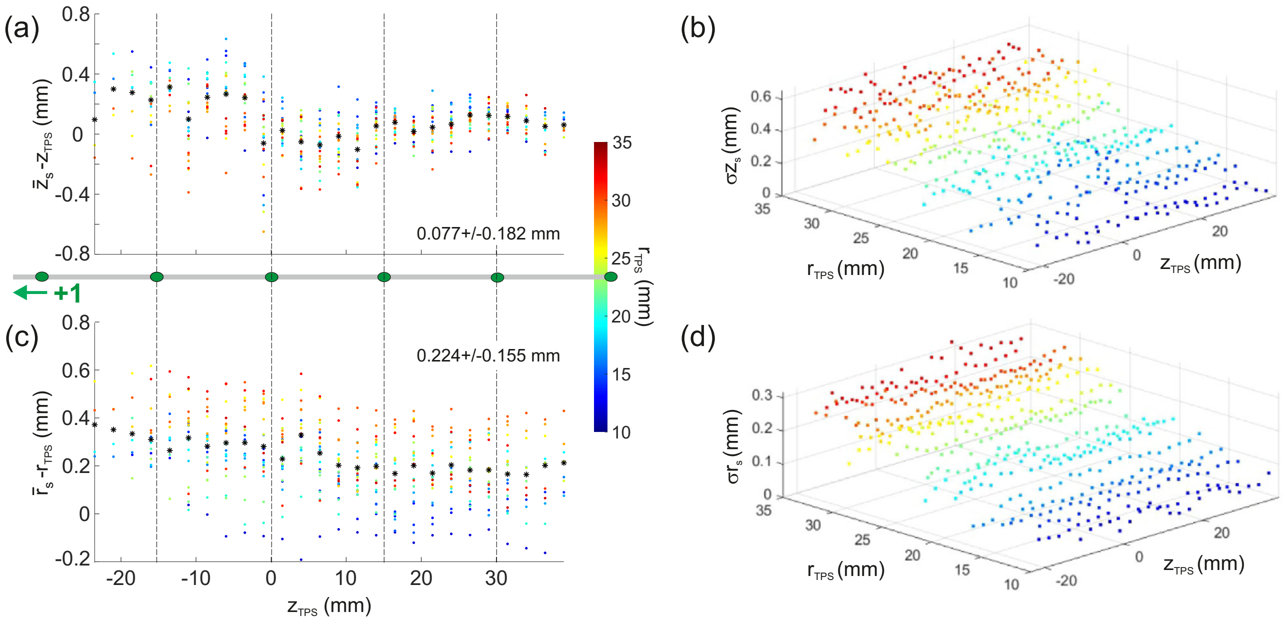

FIGURE 5 (a) and (c) Deviations $\bar{z}_s - z_{TPS}$ and $\bar{r}_s - r_{TPS}$ between measured and planned dwell positions, shown as a function of the planned axial coordinate z_{TPS}. Data points are color-coded by r_{TPS}. Black markers indicate the mean deviation at each z_{TPS}. A schematic at the bottom of (a) illustrates that the origin of the *z*-axis is arbitrarily defined at the fourth scintillation cell from the detector tip. Only six of the seven probes are shown, the position of the missing probe along the detector is indicated by a green arrow labeled "+1." Vertical lines mark the positions of each scintillation cell to facilitate spatial reference. (b) and (d) Standard deviations of $\bar{z}_s$ and $\bar{r}_s$, representing the 7SD's positional uncertainty throughout the treatment plan. 7SD, seven-probe scintillator detector.

TABLE 2 Analysis of the 7SD dwell identification as a function of dwell time values.

Dwell time	Number of dwells	Number of errors	Identification rate (%)
0.1	24	19	20.8
0.2	24	0	100
0.3	24	0	100
0.4	47	1	97.9
> 0.4	3921	0	100
Total	**4040**	**20**	**99.5**

identified, except for one position that was missed due to a time lag in the detection system [12]. For dwell times of 0.1 seconds, the identification rate was approximately 21%.

3.2 | Dwell position verification

Deviations between the planned dwell positions, (r_{TPS}, z_{TPS}), and the measured dwell positions, ($\bar{r}_s, \bar{z}_s$), were assessed for each coordinate. Each point in Figure 5a,c represents the average deviation calculated from all measured dwell positions at the same (r_{TPS}, z_{TPS}) coordinates. Overall, the measured dwell position coordinates $\bar{r}_s$ and $\bar{z}_s$ deviated from the planned values by 0.224 ± 0.155 and 0.077 ± 0.181 mm, respectively.

The uncertainty shown in Figure 5b,d was quantified as the standard deviation (SD) of the distribution of the instantaneous source position coordinates (r_s, z_s), detected at a sampling rate of 0.06 s. This analysis accounted for the cumulative dwell times at each spatial coordinate corresponding to repeated dwell positions, resulting from multiple treatment sequences conducted at the same needle locations. The uncertainty of the 7SD to locate the instant source position was less than 0.3 mm along the *r*-axis and 0.5 mm along the *z*-axis, respectively.

3.3 | Dwell time verification

Figure 6 shows the percentage distribution of deviations between measured and planned dwell times. A total of 89.4%, 97.1% and 98.9% of the data points fall within one, two, and three integration times of the camera, respectively. Note that about 50 data points exceeded three acquisition times of camera. These deviations are attributed to time lag issues in the acquisition system, resulting from the camera and data storage being managed by the same computer under Windows environment[12]. When all identified dwell positions are

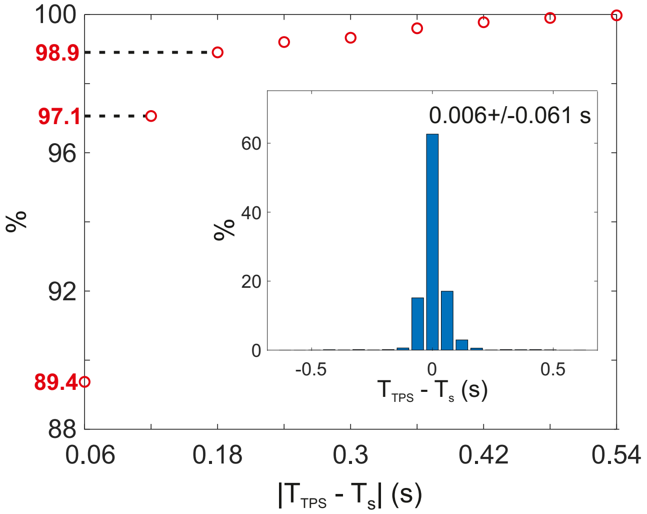

FIGURE 6 Cumulative percentage of dwell time offsets between the measured dwell times T_s and the corresponding planned dwell times T_{TPS} falling within successive harmonics of the camera's integration time. Inset: percentage distribution of the dwell time offsets.

considered, including erroneous points, the mean deviation from the planned dwell times is calculated as 0.006 ± 0.061 s.

3.4 | Reliability evaluation

3.4.1 | Systematic analysis

Figure 7 shows that for dwell times exceeding 2 s, the 7SD maintains a source position accuracy better than 1 mm across source-probe spacings from 10 to 36 mm. For dwell times between 0.9 and 2 s, the 7SD ensures this accuracy within a spacing range of 10—30.4 mm. Similarly, for dwell times between 0.3 and 0.9 s, and for dwell times below 0.2 s, the maximum reliability threshold is maintained for source-probe spacings of 10–28.3 and 10–25 mm, respectively.

3.4.2 | Treatment plan

Figure 8 presents an analysis of the offsets R_{dwell} between the measured and planned dwell positions across the entire treatment plan. The shaded areas highlight dwell positions which deviate by more than 1 mm from the planned locations. Figure 8a shows that 88.3%, 96.7% and 99.4% of the measured dwell positions exhibit deviations R_{dwell} below 0.5 mm, 0.75 mm and 1 mm, respectively. Figure 8b indicates that the highest concentration of dwell positions is observed at an offset R_{dwell} of 0.3 mm. Figure 8c shows that approximately 96% of deviations exceeding 1 mm occur at the first dwell position of the treatment sequences (dwell #1). This proportion remains at 91% for deviations larger than 0.77 mm.

3.5 | Detection of needle mispositioning

3.5.1 | Needle shift

Figure 9 illustrates the shift Δz between the correctly positioned source needle and its deliberately mispositioned counterpart along the z-axis. On average, the intended needle shifts of 1, 2, and 3mm were measured as $1.19 \pm 0.27, 2.20 \pm 0.38,$ and 2.90 ± 0.28 mm, respectively, across the evaluated source travel range.

3.5.2 | Needle tilt

The monitoring of a treatment sequence with a tilted source needle is presented in Figure 10. The three distinct needle tilt configurations are addressed in Figure 10a–c, respectively, and are depicted in the figure insets. The tilt analysis was conducted by measuring the source-probe distance, r, as a function of the planned altitude, z_{TPS}. The resulting functions, $r = f(z)$, exhibit a near-linear trend, with a little systematic curvature. The first dwell position of the treatment sequences is located at an altitude of $z = 39$ mm, which is 7 mm above the bottom solid-water template, cf. Figure 3a,b. A systematic deviation is observed from the straight line connecting the two insertion holes in the top and bottom templates through which the source needle passes (shown in red in the figures). In all cases, as the source moves away from the bottom template, the measured points progressively deviate from the inter-hole connection lines, with the recorded r values consistently exceeding those predicted by the theoretical straight path.

4 | DISCUSSION

4.1 | Dwell identification

The missed dwell position for dwell times larger than 0.2 s resulted from a time lag in the detection system, attributed to a Windows environment managing both camera control and data acquisition. To overcome lag issues, the camera and data recording processes should operate independently, each managed by a separate system, such as using a microcontroller or FPGA (Field-Programmable Gate Array) to control the camera, and a computer dedicated to handling data recording.

4.2 | Dwell position verification

The slight increase in deviation from the planned source coordinates observed in Figure 5a,c for source altitudes below 7 mm can be attributed to a minor tilt of the source needle, the source tracking algorithm, or a slight misalignment (of 0.22 mm maximum) of the seven probes

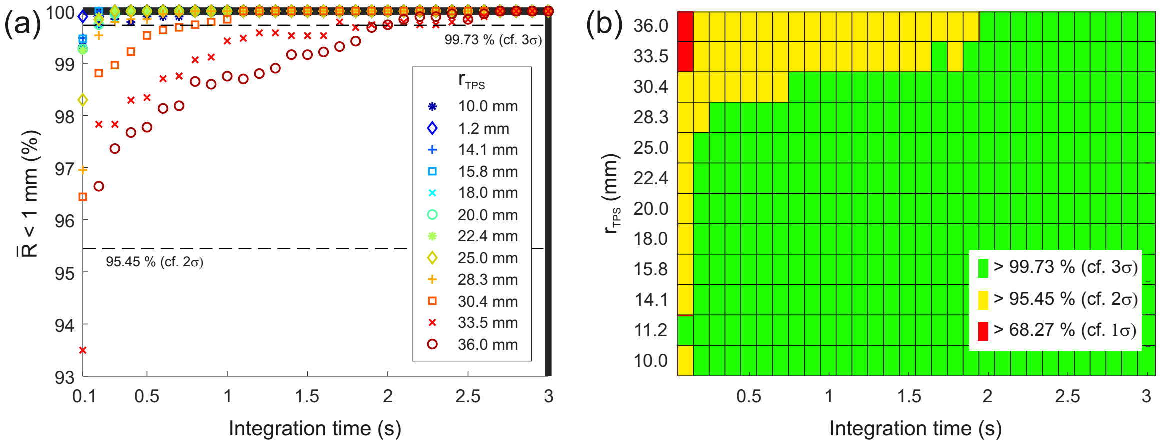

FIGURE 7 (a) Fraction of average source position offsets, $\bar{R}$, that fall below the defined reliability criterion of 1 mm. These fractions were computed for integration times ranging from 0.1 to 3 s, in 0.1-s increments, and for planned source-probe spacings (r_{TPS}) spanning from 10 to 36 mm. The reliability thresholds of 99.73% and 95.45% are superimposed on the plot for reference. These criteria correspond to the 3σ and 2σ confidence intervals of a standard normal distribution, respectively. (b) reliability level of the 7SD as a function of the planned source-probe spacing, r_{TPS}, and the integration time used to calculate $\bar{R}$. The reliability is color-coded into three levels, indicating the fractions of average position offsets $\bar{R}$ below 1 mm that are larger than 99.3%, 95.45%, and 68.27% (see legend).

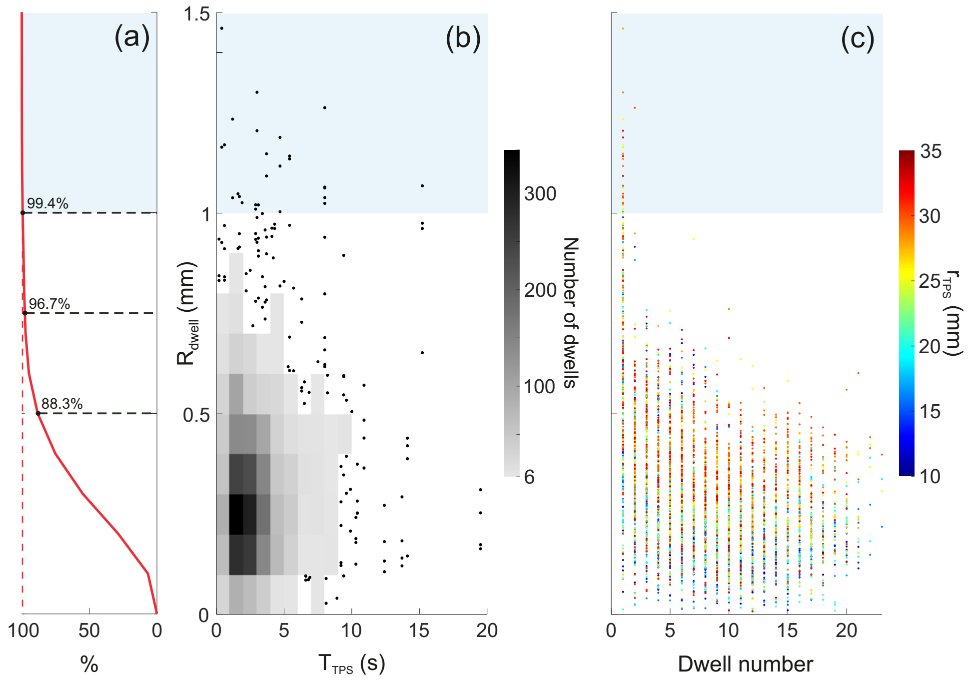

FIGURE 8 (a) Cumulative distribution of measured dwell positions as a function of their overall deviations R_{dwell} from the treatment plan. (b) Overall offsets R_{dwell} of the 4040 measured dwell positions relative to their planned positions, plotted versus the corresponding planned dwell times (T_{TPS}). The number of dwell positions is represented using a gray-scale color map, binned in intervals of 1 s for T_{TPS} and 0.1 mm for R_{dwell}. When the number of dwell positions within a bin is less than or equal to 5, individual data points are shown instead.(c) Overall offsets R_{dwell} as a function of the dwell numbers within the treatment sequences and the planned source-probe spacing, r_{TPS}, highlighting the relationship between sequential dwell positions and their deviations. r_{TPS} is color-coded (see colorbar). Dwell #1 is the first dwell of each treatment sequence.

at the end of the 7-fiber bundle forming the 7SD. However, this variation in detection accuracy, which remains within 0.2 mm, is well bellow the reliability requirement of HDR-BT [30]. Overall, the deviation from the planned dwell positions stays below 0.6 mm for both x and z. Linares et al., using a similar triangulation approach, reported source position deviations of up to 1.6 mm along z and 0.9 mm along r over a 62 mm source displacement range, with dwell times limited to 10 s, albeit at a shorter source-probe spacing of 5 mm [18]. At such close proximity, higher fluctuations in source localization are expected due to the steep dose gradient near the source.

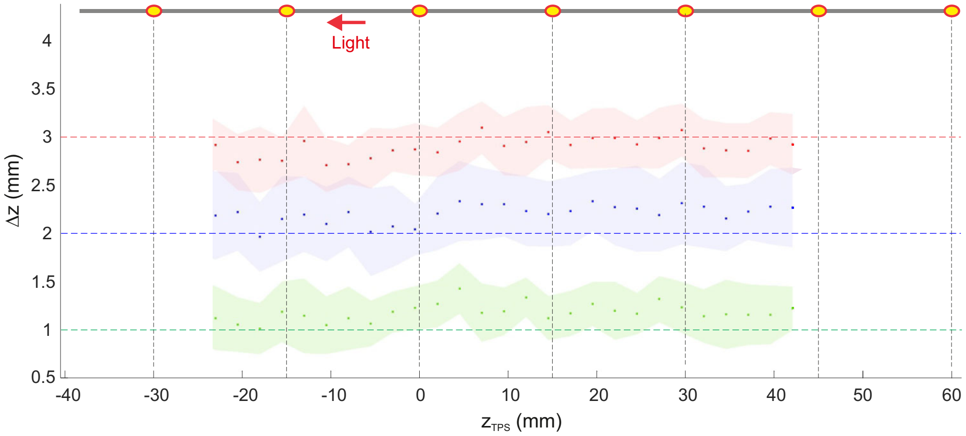

FIGURE 9 Identification of source needle mispositioning: the deliberate needle shift, Δz, is plotted as a function of the planned dwell position along the z-axis (z_{TPS}). The predicted needle shifts of 1, 2, and 3 mm are represented by dashed lines, while the measured shifts are shown as square markers spaced at 2.5 mm intervals. The shaded areas indicate the standard deviation of the instantaneous source position across each 3.7-s dwell time of the treatment sequence. Vertical dashed lines indicate the probe positions, accompanied by a schematic of the detector at the top of the figure for reference, facilitating the localization of the analysis region relative to the 7SD. The treatment length and location remain consistent with the previous analyses. 7SD, seven-probe scintillator detector

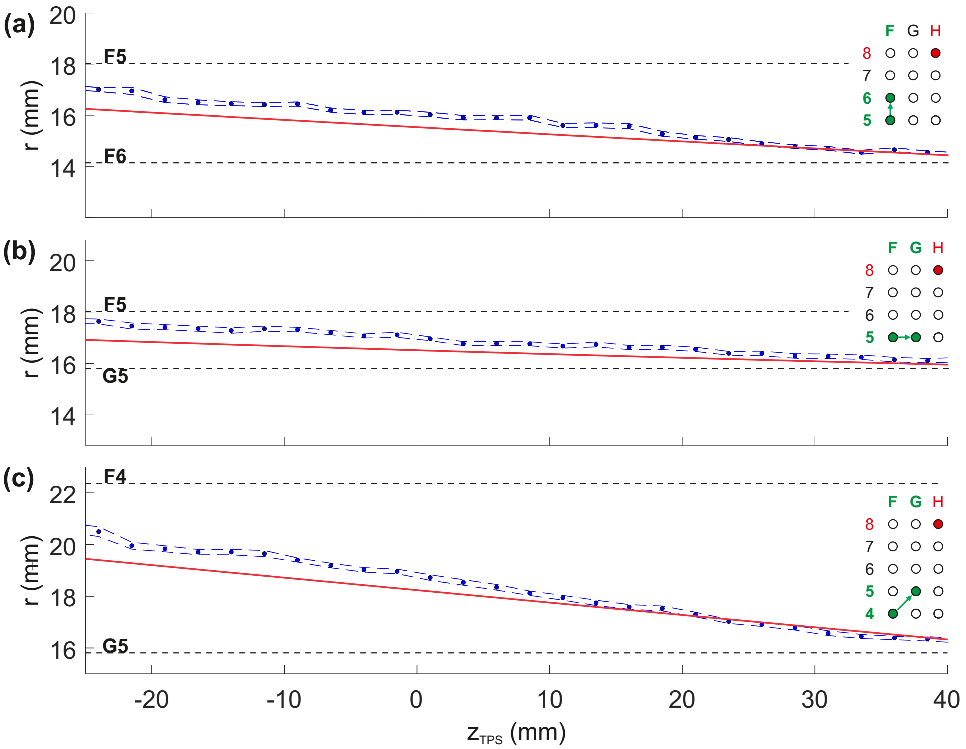

FIGURE 10 Identification of source needle mispositioning: the deliberate needle tilt is analyzed by plotting the radial distance, r, of the source from the detector as a function of the planned dwell position, z_{TPS}, along the z-axis. The tilted source trajectory results from the tilted needle passing through the following hole pairs in the top and bottom templates: (a) F5 and F6, (b) F5 and G5, and (c) F4 and G5. Schematics of the corresponding tilt configurations within the templates are shown in the insets of each figure, with the 7SD consistently positioned in hole H8 of both the top and bottom templates. The horizontal black dashed lines indicate the distance between the probe hole (H8) and the two needle insertion holes, providing reference limits for the source travel range along r. Measured dwell positions are represented by blue points, while the blue dashed lines indicate measurement accuracy, quantified by the standard deviation of the instantaneous source position relative to the average dwell position. The red lines represent the theoretical straight path connecting the insertion holes through which the source needle passes.

In previous work, we demonstrated that a six-probe detector achieves comparable accuracy in dwell position determination at both 5.5 and 10 mm source-probe spacings for 1D source tracking along the *z*-axis with 10 s dwell times. Therefore one could expect similar performances of the 7SD at 5.5 and 10 mm from the source.

The enhanced performance of our system is mainly due to its smaller scintillating detection volumes, between 110 and 280 times smaller than those used by Linares et al.[18,31], combined with a larger number of probes in our setup. This higher number of probes likely accounts for the consistent accuracy observed in the determination of the axial coordinate (z) (see Figure 5c). A slight decrease in the accuracy of radial coordinate (r) determination was observed as the source-probe spacing increased, in line with the anticipated reduction in SNR [32].

Expanding the number of probes is key to maintaining consistent accuracy in source position determination over source travel ranges extending beyond several centimeters. For instance, the three-point detector developed by Linares et al. showed source tracking accuracy that varied significantly with the source's displacement along the detector at dwell times of 10 seconds [18]. In contrast, our previous results demonstrated that a six-probe detector eliminated this position dependence at identical dwell times [20], and the present study shows that such dependence remains negligible even for treatments involving dwell times as short as 0.1 s.

The tracking accuracy of the 7SD is closely influenced by the detector's SNR and the dwell time. Figure 5b,d, which assess the precision of the 7SD in tracking the instantaneous source position, demonstrate that the SNR is predominantly dependent on the source-probe spacing r_{TPS}. The noise level remained nearly constant throughout the entire range of the source's motion, irrespective of the values of r_{TPS}.

4.3 | Dwell time measurement

On average, we observed similar performance to our previously developed single-probe detector, which shared the same probe geometry and detection architecture [12]. The main improvement in this study lies in the extension of the source-probe spacing r_{TPS} from 20 mm, as previously reported, to 36 mm. Dwell time measurement relies on detecting signal edges between successive plateaus in the characteristic staircase-like temporal profile. This process is highly dependent on both the dose gradient and the inter-dwell spacing, which influence the sharpness and amplitude of these edges. As the source-probe spacing increases, both the dose gradient and the SNR decrease, leading to reduced edge detection capability and, consequently, less accurate dwell time measurements. The expanded monitoring range achieved here, using probes with the same individual performance, underlines the value of the 7SD's multiprobe design. By leveraging seven independent probes simultaneously, the 7SD effectively multiplies the detection volume without compromising spatial resolution through volume averaging. This configuration allows for reliable dwell time verification over a broader range of source-probe spacings, reinforcing the potential of the detector for HDR-BT monitoring.

Across the entire range of source-probe spacings from 10 to 36 mm, with dwell times varying between 0.1 s and 19.5 s and an inter-dwell spacing of 2.5 mm, we measured an average deviation from the planned dwell times of 0.006 ± 0.061 s. In comparison, Guiral et al. [14] reported a deviation of 0.05 ± 0.9 s using a four-probe detector, with measurements performed at approximately 20 mm source-probe spacing, a detection interval of 0.1 s, 5-s dwell times, a source travel range of 60 mm, and an inter-dwell spacing of 2.5 mm. Additionally, Linares et al. [18] reported a deviation of 0.33 ± 0.37 s at a source-probe spacing of 5.5 mm, using 1-s dwell times and 1-mm inter-dwell spacing.

4.4 | Reliability

4.4.1 | Systematic analysis

In the context of the systematic analysis of the probes's reliability (Figure 7), the parameters $\bar{R}$ and integration time serve as analogs for dwell positions and dwell times, respectively, offering a comprehensive evaluation of the system's performance under clinically relevant conditions. We intentionally restricted the range of source-probe spacings to between 10 and 36 mm to cover the majority of prostate HDR-BT treatment volumes. In its current configuration, the 7SD detection system can potentially monitor treatments at larger source-probe spacings r_{TPS}, but with the limitation that only dwell times longer than 2 s can be reliably tracked.

For source-probe distances beyond 36 mm, extending the camera acquisition time offers a straightforward way to compensate for reduced SNR and improve detector reliability. However, this adjustment limits the system's capacity to accurately detect shorter dwell times (e.g., under 0.5 s). An alternative solution could involve replacing the sCMOS camera with seven high-sensitivity detectors, such as photomultiplier tubes, to substantially boost SNR and expand the spatiotemporal monitoring volume. Finally, the spatiotemporal monitoring volume could be significantly expanded by deploying at least two 7SDs, positioned several centimeters apart and fabricated from the same fiber bundle. The camera is particularly well-suited for this application, as it can simultaneously read signals from a large number of probes, regardless of their spatial arrangement. This enables the design of highly flexible multiprobe detection configurations without the need to modify the optical detection system itself. Moreover, such a setup would facilitate 3D source localization through triangulation techniques[19]. Therefore, viable strategies are available to achieve optimal detection reliability across the treatment volumes and the full spectrum of dwell times used in most HDR-BT procedures.

4.4.2 | Treatment plan

Under treatment plan conditions, 99.4% of the identified dwells were located with an error below the 1-mm reliability threshold, even with dwell times as short as 0.1 s (Figure 8a). Surprisingly, the largest dwell position offsets were not observed at the shortest dwell times but rather within the dwell time range between 1 and 15 s (Figure 8b). Figure 8c shows that, with a single exception, all deviations exceeding the 1-mm reliability threshold occurred at the initial dwell position (dwell #1) of the treatment sequences. Specifically, 30.4% and 8.9% of the dwell #1 positions displayed offsets exceeding 0.77 and 1 mm, respectively. These rates drop to 1.4% and 0.35% for the second dwell positions (dwell #2), with no further dwell positions surpassing the 0.77 mm threshold. The clustering of data points exceeding 0.77 mm for dwell #1 suggests a potential positioning error of the afterloader specifically occurring at the initial dwell position of the treatment sequences. Further investigation is warranted to determine whether this afterloader positioning error is systematic. Excluding these critical dwell positions, the 7SD achieved 100% reliability across the five prostate HDR-BT treatment plans assessed in this study.

The positioning error was initially suspected to stem from the detector itself. To verify this, a second, independently fabricated 7SD was tested following the same measurement protocol. The error was consistently reproduced, suggesting that the discrepancy originates from the afterloader. Moreover, it is unlikely that our detector would systematically report a deviation exclusively at the first dwell position of each sequence while maintaining higher submillimeter accuracy for all remaining positions.

4.5 | Detection of needle mispositioning

4.5.1 | Needle shift

The discrepancy between the planned and measured needle shifts remained within the measurement uncertainty of the 7SD (indicated by the standard deviation shown in the shaded area of Figure 9) and the positional accuracy of the afterloader[33]. These findings confirm that the 7SD can reliably detect and monitor needle shifts on the millimeter scale.

4.5.2 | Needle tilt

The systematic position-dependent deviation from the straight line connecting the two insertion holes, which diminishes as the dwell positions approach the bottom template, reflects the S-shaped bending of the needle caused by the insertion misalignment. The 7SD demonstrates sufficient accuracy to clearly detect sub-millimeter amplitude bending along the interstitial needle.

4.6 | Uncertainty budget

See Table 3. The expanded uncertainty ($k = 3$), corresponding to a 99.7% confidence level within a normal probability distribution, remains around 1 mm, closely matching the reliability performance of the 7SD, where 100% of the dwell positions were measured with an offset of less than 1 mm from the planned dwell positions (cf. Figure 8a).

4.7 | Clinical use

Having passed cytotoxicity testing and confirmed as biocompatible, the 7SD is well-suited for clinical use in HDR brachytherapy. Its compact dimensions allowed insertion into a biocompatible plastic sheath narrower than standard interstitial needles, making it compatible with most HDR-BT needles and catheters, including integration into clinical applicators.

Further studies are needed to evaluate the probe's performance under a broader range of clinical conditions, particularly when using sources approaching the end of their clinical lifespan (around 3 to 4 months). In such scenarios, reduced source activity results in lower SNR and necessitates longer dwell times to deliver the prescribed dose. These additional investigations will help validate the 7SD's reliability and effectiveness in lower-activity treatments. Notably, although a lower SNR can increase the uncertainty in the instantaneous source position—evident through a higher standard deviation of the signals—it has minimal impact on the accuracy of the overall dwell position for longer dwell times, where multiple measurements are averaged. In contrast, shorter dwell times, with fewer data points, are more vulnerable to reduced SNR.

We established a stringent reliability threshold for the 7SD, requiring that 99.7% of the dwell position deviations stay within 1 mm (equivalent to 3σ of a normal distribution), to anticipate additional uncertainties in clinical HDR-BT monitoring that may alter the probe. Although our study used a single-needle setup, clinical prostate brachytherapy typically involves multiple manually-implanted needles, which could alter the

TABLE 3 Uncertainty budget for dwell time and position verification, as presented by Andersen et al.[5].

		Dwell position uncertainty (mm)	Dwell time uncertainty (s)	Type	Source
Detector	Repeatability				
	(0z)	0.182	—	A	Figure 5
	(0r)	0.155	—	A	Figure 5
	—	—	0.061	A	Figure 6
	Scint. temp. (17–19°C)				
	(0z)	0.015	—	B	Ref. 25, Sec. 2.3
	(0r)	0.010	—	B	Ref. 25, Sec. 2.3
	Stem effect	0	0	B	Sec. 2.1.4
	Integration time	—	0.017 (0–0.06)	B	Sec. 2.1.4
	Total	**0.240**	**0.063**		
Needle/detector mispositionning	Needle/(0r)	0.029 (±0.05)	—	B	Sec. 2.1.2
	Detector/(0r)	0.104 (0.18)	—	B	Sec. 2.1.2
	Total	**0.108**	—		
Afterloader	Source position/(0z)	0.231 (±0.4)	0.058 (±0.1)	B	Ref. 33
Overall (k=1 – 68.3%)		**0.350**	**0.086**		
Overall (k=3 – 99.7%)		**1.050**	**0.258**		

Note: In accordance with ISO (1995) guidelines, uncertainties are classified into two categories: Type A, which are evaluated using valid statistical methods, and Type B, which are based on scientific judgment and available information. A Type B uncertainty, u, is calculated as $u = (v_{\max} - v_{\min})/\sqrt{12}$, where $v_{\max}$ and $v_{\min}$ represent the maximum and minimum values, respectively. The total combined uncertainty, u_{tot}, for a series of uncertainties (u_i, where $i \in N$), is determined by $u_{\text{tot}} = \sqrt{\sum_i u_i^2}$.

local energy distribution and attenuate the 7SD signal. Moreover, the accuracy of in vivo HDR-BT monitoring is highly dependent on the positional stability of the 7SD, which could be affected by anatomical shifts during the treatment [1]. This limitation would likely be alleviated in applicator-based brachytherapy, where both the source and detector catheters would be securely fixed relative to each other, reducing the potential for positional drifts. Additionally, triangulation algorithms could be refined using x-ray, MRI, or ultrasound imaging, which are routinely used to visualize needles or catheters in vivo, either in real time or during pre- and post-treatment assessments.

In its current configuration, the 7SD offers a monitoring volume sufficient for most HDR-BT clinical applications. However, its lateral detection range may be limited in cervical cancer treatments requiring complex applicators with laterally positioned implantation needles. Several strategies described in Section 4.4.1 could be employed to broaden the detection volume for these challenging geometries. Although the 7SD's monitoring field fully covers the prostate HDR-BT treatment volume when placed at the center of the BT template (cf. Figure 3c), this approach may not be clinically feasible for the smaller prostates, where all central template holes are required for treatment needles, leaving no available space for detector placement [34]. Therefore, as outlined in Section 4.4.1, more advanced configurations incorporating at least two 7SD detectors placed at the periphery of the treatment volume could be used to perform remote monitoring throughout the tumor region. This setup would also enable 3D source localization via triangulation techniques [19].

The proposed multiprobe detection strategy provides outstanding flexibility and scalability, enabling the development of optimized detection systems for a wide variety of HDR-BT techniques. By adjusting parameters such as inter-probe spacing, the number of probes per detector, and the overall number of detectors, the system can be tailored to meet specific clinical requirements. Probes may be integrated into a single fiber bundle, multiple bundles, or distributed separately. The camera-based readout system maximizes modularity and scalability by supporting a wide range of detection configurations—with varying probe numbers and architectures—using a single optical sensor.

Brachytherapy encompasses a wide range of clinical scenarios, from straightforward treatments using rigid applicators to more complex procedures involving free-hand needle implantation guided by online per-fraction imaging. The proposed system is adaptable to all these situations, with varying levels of integration required with the TPS. In simpler cases involving fixed applicators, a one-time export of the planned dwell positions from the TPS is sufficient for comparison with the measured source positions. In more complex implantations, such as those involving irregular or non-rigid needle placement, knowledge of the detector-carrying needles' positions becomes critical for refining the triangulation-based source localization algorithm. In such contexts, real-time communication with the TPS or imaging system is required, and full integration into the TPS workflow could be envisioned as a future enhancement.

5 | CONCLUSION

We presented the performance of a 7SD system for time-resolved HDR-BT monitoring across a broad range of dwell times (0.1–19.5 s), a 62 mm source travel distance, and source-detector spacings up to 36 mm. Compared to single-probe detectors [12], the 7SD's multi-probe design significantly expands the monitoring volume both axially and radially and enables accurate 2D source tracking through triangulation, defining state-of-the-art performance levels. The detector's biocompatibility was confirmed through cytotoxicity testing. Of the 4040 dwell positions analyzed in this study, 99.5% were successfully identified, with a 100% identification rate for dwell times exceeding 0.2 s. On average, dwell position determination achieved an accuracy of 0.224 ± 0.155 mm along the source displacement axis and 0.077 ± 0.181 mm in the orthogonal radial direction. The mean deviation from planned dwell times was 0.006 ± 0.061 s. A high reliability level was demonstrated, with 99.4% of all dwell positions measured within the 1 mm threshold. The remaining 0.6% of deviations, consistently observed at the initial dwell positions of treatment sequences, appear to result from a systematic source positioning error by the afterloader. The consistent accuracy of the 7SD across the entire source travel range enables the detection of subtle afterloader malfunctions, providing a precise and valuable tool for assessing the integrity of HDR-BT clinical setups and procedures. Additionally, the detector precisely identified intentional needle mispositioning scenarios, including both shifts and tilts, with submillimeter accuracy. This study demonstrates that the proposed 7SD system is well-suited for use as an in vivo detector for time-resolved HDR-BT treatment monitoring. It delivers state-of-the-art performance while offering exceptional flexibility and scalability to accommodate a wide range of HDR-BT treatment scenarios.

ACKNOWLEDGMENTS

This work has received funding from the SAYENS Agency, the French Agence Nationale de la Recherche under project NANOPTiX (ANR-18-CE42-0016), the EQUIPEX+ SMARTLIGHT platform (ANR-21-ESRE-0040), the EQUIPEX+ NANOFUTUR (ANR-21-ESRE-0012) and the EIPHI Graduate School (ANR-17-EURE-0002). This work was also supported by the French Renatech network, MIMENTO technological facility, and the Région Bourgogne Franche-Comté.

CONFLICT OF INTEREST STATEMENT

The authors declare no conflicts of interest.

REFERENCES

1. Fonseca GP, Johansen JG, Smith RL, et al. In vivo dosimetry in brachytherapy: requirements and future directions for research, development, and clinical practice. *Phys Imaging Radiat Oncol*. 2020;16:1-11.
2. Verhaegen F, Fonseca GP, Johansen JG, et al. Future directions of in vivo dosimetry for external beam radiotherapy and brachytherapy. *Phys Imaging Radiat Oncol*. 2020;16:18-19.
3. Lambert J, McKenzie D, Law S, Elsey J, Suchowerska N. A plastic scintillation dosimeter for high dose rate brachytherapy. *Phys Med Biol*. 2006;51:5505.
4. Lambert J, Nakano T, Law S, Elsey J, McKenzie DR, Suchowerska N. In vivo dosimeters for HDR brachytherapy: a comparison of a diamond detector, MOSFET, TLD, and scintillation detector. *Med Phys*. 2007;34:1759-1765.
5. Andersen CE, Nielsen SK, Greilich S, Helt-Hansen J, Lindegaard JC, Tanderup K. Characterization of a fiber-coupled luminescence dosimetry system for online in vivo dose verification during brachytherapy. *Med Phys*. 2009;36:708-718.
6. Belley MD, Craciunescu O, Chang Z, et al. Real-time dose-rate monitoring with gynecologic brachytherapy: Results of an initial clinical trial. *Brachytherapy*. 2018;17:1023-1029.
7. Johansen J, Kertzscher G, Jørgensen E, et al. Dwell time verification in brachytherapy based on time resolved in vivo dosimetry. *Phys Med*. 2019;60:156-161.
8. Kertzscher G, Andersen CE, Siebert F-A, Nielsen SK, Lindegaard JC, Tanderup K. Identifying afterloading PDR and HDR brachytherapy errors using real-time fiber-coupled Al2O3: C dosimetry and a novel statistical error decision criterion. *Radiother Oncol*. 2011;100:456-462.
9. Jørgensen EB, Johansen JG, Overgaard J, et al. A high-Z inorganic scintillator-based detector for time-resolved in vivo dosimetry during brachytherapy. *Med Phys*. 2021;48:7382-7398.
10. Johansen JG, Rylander S, Buus S, et al. Time-resolved in vivo dosimetry for source tracking in brachytherapy. *Brachytherapy*. 2018;17:122-132.
11. Jørgensen EB, Kertzscher GK, Buus S, et al. Accuracy of an in vivo dosimetry-based source tracking method for afterloading brachytherapy-a phantom study. *Med Phys*. 2021;48:2614-2623.
12. Gonod M, Suarez MA, Avila CC, et al. Characterization of a miniaturized scintillator detector for time-resolved treatment monitoring in HDR-brachytherapy. *Phys Med Biol*. 2022;67:245016.
13. Wang R, Ribouton J, Pittet P, Guiral P, Jalade P, Lu G-N. Implementation of GaN based real-time source position monitoring in HDR brachytherapy. *Radiat Meas*. 2014;71:293-296.

14. Guiral P, Ribouton J, Jalade P, et al. Design and testing of a phantom and instrumented gynecological applicator based on GaN dosimeter for use in high dose rate brachytherapy quality assurance. *Med Phys*. 2016;43:5240-5251.
15. Cartwright L, Suchowerska N, Yin Y, Lambert J, Haque M, McKenzie D. Dose mapping of the rectal wall during brachytherapy with an array of scintillation dosimeters. *Med Phys*. 2010;37:2247-2255.
16. Therriault-Proulx F, Briere TM, Mourtada F, Aubin S, Beddar S, Beaulieu L. A phantom study of an in vivo dosimetry system using plastic scintillation detectors for real-time verification of 192Ir HDR brachytherapy. *Med Phys*. 2011;38:2542-2551.
17. Therriault-Proulx F, Beddar S, Beaulieu L. On the use of a single-fiber multipoint plastic scintillation detector for 192Ir high-dose-rate brachytherapy. *Med Phys*. 2013;40:062101.
18. Linares Rosales HM, Archambault L, Beddar S, Beaulieu L. Dosimetric performance of a multipoint plastic scintillator dosimeter as a tool for real-time source tracking in high dose rate Ir brachytherapy. *Med Phys*. 2020;47:4477-4490.
19. Linares Rosales HM, Johansen JG, Kertzscher G, Tanderup K, Beaulieu L, Beddar S. 3D source tracking and error detection in HDR using two independent scintillator dosimetry systems. *Med Phys*. 2021;48:2095-2107.
20. Gonod M, Suarez MA, Avila CC, et al. Six-probe scintillator dosimeter for treatment verification in HDR-brachytherapy. *Med Phys*. 2023;50:7192-7202.
21. Qin Z, Hu Y, Ma Y, et al. Embedded structure fiber-optic radiation dosimeter for radiotherapy applications. *Opt Express*. 2016;24:5172-5185.
22. Hu Y, Qin Z, Ma Y, et al. Characterization of fiber radiation dosimeters with different embedded scintillator materials for radiotherapy applications. *Sens Actuators A Phys*. 2018;269:188-195.
23. Alharbi M, Gillespie S, Woulfe P, McCavana P, O'Keeffe S, Foley M. Dosimetric characterization of an inorganic optical fiber sensor for external beam radiation therapy. *IEEE Sens J*. 2018;19:2140-2147.
24. O'Reilly D, Qayyum K, Alharbi M, Foley M. Temperature Dependence of Novel Inorganic Scintillation Detectors. In: *2020 IEEE Sensors*, Rotterdam, Netherlands, 2020:1-4.
25. McLaughlin O, Martyn M, Kleefeld C, Foley M. Investigation of temperature dependence of inorganic scintillators using the HYPERSCINT research platform. *Radiat Meas*. 2023;164:106936.
26. Suarez MA, Lim T, Robillot L, et al. Miniaturized fiber dosimeter of medical ionizing radiations on a narrow optical fiber. *Opt Express*. 2019;27:35588-35599.
27. Gonod M, Avila CC, Suarez MA, et al. Miniaturized scintillator dosimeter for small field radiation therapy. *Phys Med Biol*. 2021;66:115016.
28. Fonseca GP, Viana RS, Podesta M, et al. HDR 192Ir source speed measurements using a high speed video camera. *Med Phys*. 2015;42:412-415.
29. Canny J. A computational approach to edge detection. *IEEE Trans Pattern Anal Mach Intell*. 1986;PAMI-8:679-698.
30. Dempsey C, Smith R, Nyathi T, et al. ACPSEM brachytherapy working group recommendations for quality assurance in brachytherapy. *Australas Phys Eng Sci Med*. 2013;36:387-396.
31. Linares Rosales HM, Duguay-Drouin P, Archambault L, Beddar S, Beaulieu L. Optimization of a multipoint plastic scintillator dosimeter for high dose rate brachytherapy. *Med Phys*. 2019;46:2412-2421.
32. Andersen CE, Nielsen SK, Lindegaard JC, Tanderup K. Time-resolved in vivo luminescence dosimetry for online error detection in pulsed dose-rate brachytherapy. *Med Phys*. 2009;36:5033-5043.
33. Robinson D. Determination of Ir-192 micrselectron-V2 HDR/PDR dwell position reproducibility using a slit camera. *Brachytherapy*. 2021;20:1334-1340.
34. Mason J, Mamo A, Al-Qaisieh B, Henry AM, Bownes P. Real-time in vivo dosimetry in high dose rate prostate brachytherapy. *Radiother Oncol*. 2016;120:333-338.

How to cite this article: Gonod M, Suarez MA, Laskri S, et al. Seven-probe fiber detector for time-resolved source tracking in HDR-brachytherapy: Pre-clinical experimental evaluation. *Med Phys*. 2025;52:e70080. https://doi.org/10.1002/mp.70080